

MR Elastography of the Human Heart: Noninvasive Assessment of Myocardial Elasticity Changes by Shear Wave Amplitude Variations

Ingolf Sack,^{1*} Jens Rump,¹ Thomas Elgeti,¹ Abbas Samani,^{2,3} and Jürgen Braun⁴

Many cardiovascular diseases and disorders are associated with hemodynamic dysfunction. The heart's ability to contract and pump blood through the vascular system primarily depends on the elasticity of the myocardium. This article introduces a magnetic resonance elastography (MRE) technique that allows noninvasive and time-resolved measurement of changes in myocardial elasticity over the cardiac cycle. To this end, low-frequency shear vibrations of 24.3 Hz were induced in the human heart via the anterior chest wall. An electrocardiograph (ECG)-triggered, steady-state MRE sequence was used to capture shear oscillations with a frame rate of eight images per vibration cycle. The time evolution of 2D-shear wave fields was observed in two imaging planes through the short axis of the heart in six healthy volunteers. Correlation analysis revealed that wave amplitudes were modulated in synchrony to the heartbeat with up to 2.45 ± 0.18 higher amplitudes during diastole than during systole (interindividual mean \pm SD). The reduction of wave amplitudes started at 75 ± 9 ms prior to changes in left ventricular diameter occurring at the beginning of systole. Analysis of this wave amplitude alteration using a linear elastic constitutive model revealed a maximum change in the myocardial wall stiffness of a factor of 37.7 ± 10.6 during the cardiac cycle. *Magn Reson Med* 61:668–677, 2009. © 2008 Wiley-Liss, Inc.

Key words: cardiac MR elastography; shear waves; myocardium; heart mechanics; shear modulus

Heart failure is a progressive disorder in which damage to the heart causes weakening of the cardiovascular system. It has emerged as a growing health problem that is likely to reach epidemic proportions in developed countries. Among individuals aged 55 years, almost one in three will develop heart failure during their remaining lifespan. Heart failure continues to be a fatal disease, with a survival rate below 35% 5 years after the first diagnosis (1,2). Early detection of heart failure is an important prerequisite for reducing the mortality rate associated with cardiovascular impairment (3). Assessment of ventricular pressure dynamics has been found to be

crucial for the diagnosis of heart failure and the prediction of cardiovascular health risks (4). While systolic function is described by the ability of the myocardium to actively contract and thus to generate pressure, diastolic heart function is characterized by myocardial relaxation. Systolic function can be easily assessed by calculating the ejection fraction using echocardiography or magnetic resonance imaging (MRI). It has been observed that in over 50% of patients with heart failure, diastolic cardiac function is limited, while systolic function is preserved (5). Diastolic dysfunction can be the result of a large variety of diseases ranging from hypertension, diabetes, and ischemia to infiltrative diseases such as myocarditis, amyloidosis, or restrictive cardiomyopathy (6,7). Presently, it is difficult to detect dysfunction of diastolic ventricular filling noninvasively. Echocardiography and MRI can accurately determine morphology, volume, and volume fractions of the heart together with their spatial and time derivatives, strain, and velocity (8–13). MRI also demonstrates alterations in tissue composition (edema, necrosis, scar) and perfusion (7). However, the most important functional characteristic of the heart—the alteration of ventricular pressure between systole and diastole—is not amenable to assessment without techniques capable of measuring forces in response to regional myocardial pressure (14). Shear-wave-based elastography allows noninvasive palpation of tissue deep inside the body in order to assess the tissue's shear modulus, which characterizes its shear deformation resistance to harmonically oscillating shear forces (15,16). Recently, Rump et al. (17,18) demonstrated the feasibility of observing externally induced shear vibrations in the living human heart using MRI elastography (MRE). This work was based on fractional encoding of shear oscillations in the frequency range of 50 Hz using balanced steady-state free precession (bSSFP) MRE. Although the propagation of shear waves through the interventricular septum was visualized in a time-resolved fashion, wave propagation speed (and thus myocardial elasticity) was difficult to determine. The deduction of elastic moduli from shear waves by inversion algorithms, as traditionally done in MRE, is often compromised by noise and unknown boundary conditions. These effects are mitigated by high wave numbers. However, high wave numbers require high driving frequencies, which in turn result in strongly damped wave amplitudes due to the viscous properties of soft biological tissues. For instance, a 50-Hz vibration would result in myocardial oscillations with wavelengths of about 10 cm assuming an isotropic shear elasticity of 30 kPa (19). Such large wavelengths are not suited for determining regional myocardial stiffness by inversion-based MRE.

To address this deficiency, a technique is introduced here that measures wave amplitude variations (WAV) resulting

¹Department of Radiology, Charité-Universitätsmedizin Berlin, Berlin, Germany.

²Department of Medical Biophysics, University of Western Ontario, Ontario, Canada.

³Department of Electrical and Computer Engineering, University of Western Ontario, Ontario, Canada.

⁴Institute of Medical Informatics, Charité-Universitätsmedizin Berlin, Berlin, Germany.

Grant sponsor: German Research Foundation; Grant number: Sa/901-3.

*Correspondence to: Ingolf Sack, Ph.D., Department of Radiology, Charité-Universitätsmedizin Berlin, Charitéplatz 1, 10117 Berlin, Germany. E-mail: ingolf.sack@charite.de

Received 1 June 2007; revised 23 July 2008; accepted 8 October 2008.

DOI 10.1002/mrm.21878

Published online 18 December 2008 in Wiley InterScience (www.interscience.wiley.com).

from the superposition of externally induced vibrations and intrinsic elasticity changes. First, it is demonstrated in a phantom study that WAV-MRE is capable of determining the position and the relative amount of elasticity alteration despite the occurrence of reflections and wave damping. Second, cardiac WAV-MRE based on fractional motion encoding of low-frequency vibrations (24.3 Hz) is applied in six healthy volunteers. In this feasibility study, a very high temporal resolution of 5.16 ms achieved by segmented k -space acquisition is used to separate enforced oscillations from intrinsic heart motion. Then, the time evolution of the WAV effect (i.e., wave amplitude alterations between diastole and systole) is compared with left ventricular (LV) morphology determined by cine-MRI in the same volunteers. Finally, preliminary elastic modulus ratios between systole and diastole are presented.

THEORY

The fundamental theoretical development of this study is based on the concept of energy flow through the heart characterized by a constant flux of elastic wave energy:

$$\langle F \rangle = \langle E \rangle c = \text{const.} \quad [1]$$

where $\langle F \rangle$ and $\langle E \rangle$ denote the time average of the flux of energy and energy density. F is sometimes called the “wave intensity” in the literature, and c represents the velocity of the “flow” of energy per unit area per unit time that is transported by elastic waves. Assuming time-harmonic plane waves of amplitude U and angular driving frequency ω , the following relation can be obtained for the average of F over a wave oscillation period (20):

$$\langle F \rangle = \frac{1}{2} \rho c U^2 \omega^2. \quad [2]$$

where ρ is the density that is assumed to be 1 kg/liter in this study. A more general field representation of the elastic wave intensity that allows for compressional and transverse wave modes is given in the Appendix. Here, we continue with the assumption that U in Eq. [2] is the scalar magnitude of wave polarization \mathbf{U} given by $U = \sqrt{\sum_j U_j^2}$ $j \in \{1,2,3\}$ corresponding to the Cartesian coordinates $\{x,y,z\}$. Furthermore, $\langle F \rangle$ is considered to be transported by either compressional ($c = c_L$) or shear waves ($c = c_T$; see appendix). Equation [2] shows that the time average of the intensity of the waves depends on both the wave velocity and the square of polarization magnitude U . Thus, the ratio of U at two different time points, t_1 and t_2 , during the cardiac cycle equals the square root of the inverse wave-speed ratio: $U(t_1)/U(t_2) = [c(t_2)/c(t_1)]^{1/2}$. In shear-wave-based elastography, the assumption of incompressibility of soft biological tissues is well established. Mathematically, incompressibility is represented by a limit where the first Lamé coefficient λ is infinite and the ratio $c_L(t_2)/c_L(t_1)$ equals one; i.e., no wave amplitude change occurs due to compressional waves. In contrast, the ratio of shear modulus μ at t_1 and t_2 yields the following power relationship with the amplitude ratio at t_1 and t_2 :

$$\frac{\mu(t_1)}{\mu(t_2)} = \left(\frac{U(t_2)}{U(t_1)} \right)^4. \quad [3]$$

This equation provides the possibility to measure myocardial elasticity changes during the cardiac cycle based on shear wave amplitude variations. The proportionality $U^4 \sim \mu$ implies a relatively low sensitivity of shear wave amplitudes to shear modulus changes in WAV-MRE; however, given the large LV pressure change that occurs during the cardiac cycle (up to a factor of 40 [21,22]), we expect to see an amplitude variation in the order of 2.5. It will be shown that such variation is relatively easy to detect using MRE. Equation [3] represents the simplest relationship between elasticity and wave amplitude ratios. To account for spatial variations of parameters in Eq. [3], one has to consider reflections on elastic interfaces as outlined in a phantom study by Papazoglou et al. (23). In this study, we test the influence of reflections and damping on Eq. [3] using a two-layer phantom. Therefore, t is substituted by a spatial axis x with $t_1 \rightarrow x_{stiff}$ and $t_2 \rightarrow x_{soft}$ and the ratio of wave amplitudes is evaluated along x .

Evaluation of Experimental Wave Amplitudes

In cardiac MRE, oscillatory vibrations are simultaneously encoded with blood flow and intrinsic heart motion. Therefore, it is important to eliminate intrinsic contributions to the spin phase from externally induced vibrations. This goal was achieved in two steps. First, the time derivative of the spin phase signal was evaluated, which suppresses slow heart motions. Second, a correlation of the remaining phase signal with time-harmonic oscillations of the driving frequency was obtained. The latter extracts the signal oscillating with the frequency of the wave source. The time derivative of the spin phase is calculated from raw phase data $\phi(t)$ using the following equation:

$$\dot{\phi}(t) = -i \exp[-i\phi(t)] \frac{d \exp[i\phi(t)]}{dt} \quad [4]$$

This method avoids the elaborate phase unwrapping usually needed in MRE, since $\dot{\phi}(t)$ is in the range of $\in [-\infty, \infty]$, whereas the initial $\phi(t)$ is in the range of $\in [0, 2\pi]$. $\dot{\phi}(t)$ represents phase oscillations linearly scaled by their frequency. These oscillations are transformed to displacement velocity $\dot{u}_j(t)$ using a factor derived for fractional MRE by incorporating a single-cycle sinusoidal motion-encoding gradient (MEG) (17):

$$\dot{u}_j(t) = \dot{\phi}(t) \frac{\pi(1 - q^2)}{\gamma g_j \tau_g \sin(\pi q)}; \quad q = \frac{\tau_g}{\tau_v}. \quad [5]$$

In this equation, τ_v is a vibration period ($2\pi/\omega$); τ_g and g_j are the duration and amplitude of the MEG, respectively; and γ denotes the gyromagnetic ratio. The wave amplitude component U_j is obtained by calculating a complex correlation of \dot{u}_j with time-harmonic oscillations of the driving frequency:

$$U_j(T) = \frac{1}{\pi} \left| \int_T^{T+\tau_v} \dot{u}_j(t) \exp(i\omega t) dt \right| \quad [6]$$

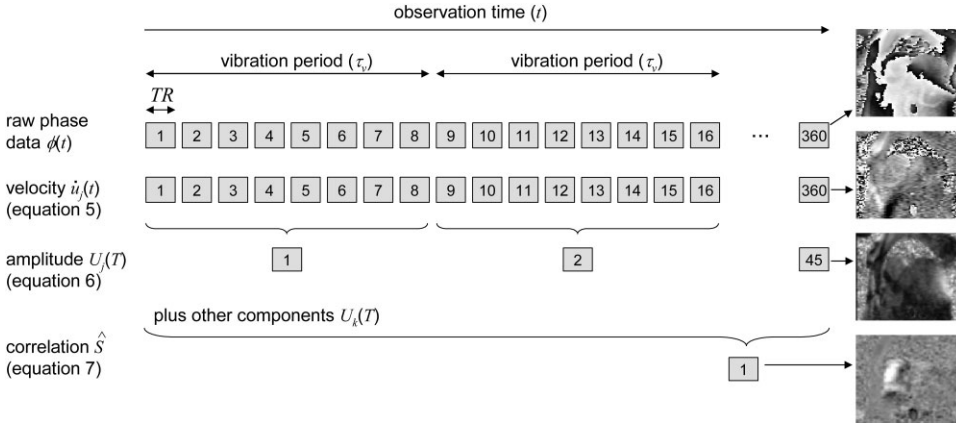


FIG. 1. Scheme of data processing used for myocardial MRE. Gray boxes indicate image data with corresponding image number. Four example images corresponding to the processing steps introduced in the Theory section are shown on the right side.

Here, the temporal resolution of $U_j(T)$ is determined by the duration of a single vibration cycle, i.e., its resolution is reduced by the number of the acquired wave images per τ_v . In our experiments, 360 images of $\dot{u}_j(t)$ were acquired within 45 vibration periods, yielding an eightfold resolution reduction in $U_j(T)$ compared to $\dot{u}_j(t)$ as shown in Fig. 1. The amplitude of $U_j(T)$ ($U(T) = \sqrt{\sum_j U_j(T)^2}$) is the quantity we use in Eq. [3] to investigate myocardial stiffness changes. Such changes occur primarily within contracting tissues. Therefore, it is important to identify regions where $U(T)$ changes during the cardiac cycle in order to identify regions of contracting myocardium and to segment them from blood and surrounding noncontracting tissues. In the following, a discrete form of $U(T)$, U_n , is analyzed by correlation \hat{S} , which is defined as follows:

$$\hat{S} = \frac{\sum_{n=1}^N U_n S_n}{\sqrt{\sum_{n=1}^N U_n^2 \sum_{n=1}^N S_n^2}} - \frac{\sum_{n=1}^N S_n}{\sqrt{N \sum_{n=1}^N S_n^2}}; \quad [7]$$

$$S = \begin{cases} 0, & t_{start_systole} \leq T \leq t_{end_systole} \\ 1, & t_{start_diastole} \leq T \leq t_{end_diastole} \end{cases}$$

Here, N is the number of points in U (45 in our experiments) and S is a step function defined on the basis of the duration of systole and diastole. For segmentation purposes, it is desirable that \hat{S} becomes nonzero (within a small range) for points within contracting tissues and zero for points corresponding to noncontracting tissues. The first term in Eq. [7] yields the normalized correlation between U_n and S_n , which is a nonzero value for contracting tissue points. For noncontracting tissues, however, the first term does not yield zeros. Consequently, the second term was subtracted, which can be shown to result in approximately zero values of \hat{S} for tissues that have a rigid body motion contaminated with noise. Therefore, in the following study, the shear modulus ratio in Eq. [3] is analyzed within regions of $\hat{S} > 0$. Figure 1 illustrates all steps of image processing applied for identifying regions of wave amplitude variations associated with myocardial contraction.

MATERIALS AND METHODS

Phantom Study

A gel phantom was constructed from two layers of Wirogel (Bego Inc., Bremen, Germany) placed in a 20-cm-long plastic tube with an 18-cm diameter. Upper (stiffer) and lower (softer) layers were made from 3% and 0.25% gel/water mixtures, respectively. In the first experiment, a vibration transducer plate (11.0×11.0 cm) was attached to the phantom's surface, while in the subsequent experiment the entire tube was vibrated. The vibration frequency in both experiments was 32.35 Hz. Both of these phantom experiments and the subsequent in vivo heart MRE experiments were conducted to test the proposed WAV-MRE technique in the presence of wave reflections and wave damping with different degrees of both effects. Experiments were run on a 1.5-T scanner (Siemens Sonata; Siemens Erlangen, Germany). A modified spin-echo echo-planar imaging (EPI) sequence (24) was used that incorporated a single-cycle sinusoidal MEG with a frequency matched to the vibration frequency. The direction of motion sensitization was consecutively changed in order to capture all vector components of the displacement field u_j . Twenty images were acquired with toggled motion sensitization gradients in each second acquisition for calculating 10 phase-difference wave images. The delay between the start of the motion and the MEG was increased with $\tau_v/10$ for each phase-difference image. The wave field magnitude, U , was determined by a temporal Fourier transformation of $u_j(t)$ using $U = \sqrt{\sum_j |u(\omega)_j|^2}$.

In Vivo Cardiac MRE

In vivo studies were performed in six healthy male volunteers aged 32, 33, 35, 35, 37, and 46 years, numbered 1–6 in the following.

A remote oscillator described in Ref. 25 was used to vibrate the chest. A 2.5- to 3.0-m-long transducer piston was mounted in the center of the oscillator membrane, while the proximal end rested on the center of the volunteer's chest, held down by its own weight (≈ 1.5 kg) (26). The vibration in the anterior–posterior (A-P) direction was synchronized to the repetition time (TR) of the MRE sequence with one sinusoidal burst of 41.28 ms in length (consistent with the 24.3 Hz driving frequency) after every eighth TR. The vibration amplitude was approximately 1.5 mm on the surface of the chest.

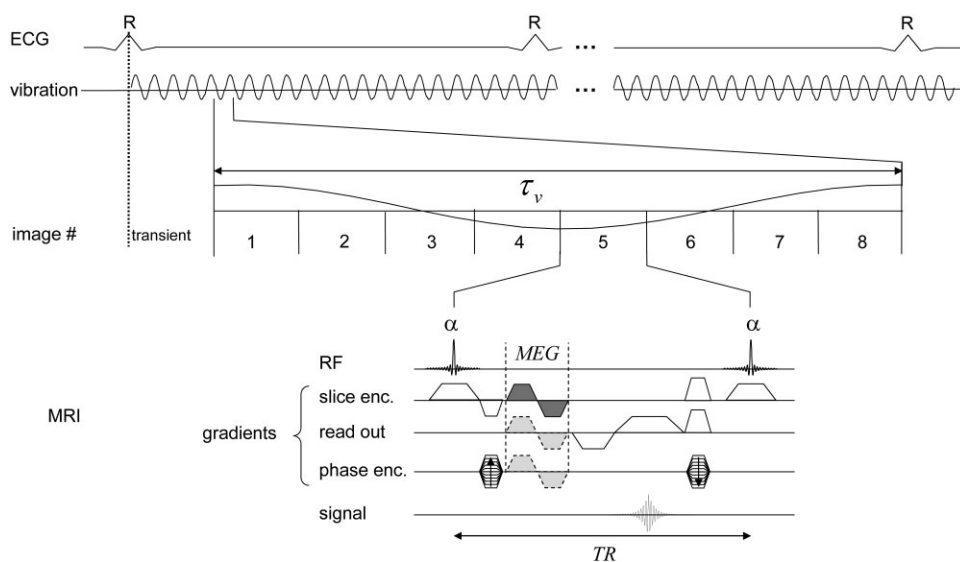


FIG. 2. MRE sequence used to measure the vibration response of myocardial tissue to low-frequency shear waves of 24.3 Hz.

A six-channel body phased-array coil was used in combination with an electrocardiograph (ECG)-gated, spoiled gradient-echo sequence (27) (flip angle of 15°) for parallel acquisition of phase-contrast wave images. Motion sensitization was achieved by a 2-ms single-cycle trapezoidal MEG between phase-encoding and readout (Fig. 2), yielding a TR of 5.16 ms. The MEG amplitude was 35 mT/m in the readout direction and 25 mT/m in the direction of phase encoding and slice selection. In the following, the Cartesian reference frame is assigned to the MRI gradient system with the vector components x_1 for readout, x_2 for phase encoding, and x_3 for slice selection (Fig. 3a). Oscillation was sequentially captured by a series of 360 phase images and a temporal resolution of 5.16 ms, resulting in an observation time of 1.86 s. During this time at least two systolic heart phases are captured; however, fewer phase images might be acquired in future applications. For sequential vibration encoding, segmented k -space acquisition was applied with one phase-encoding step per ECG trigger. A total of 34 encoding steps were needed for a full image reconstruction because we used twofold generalized autocalibrating partially parallel acquisition (GRAPPA) acceleration and interpolation of k -space from 64 to 128 lines. Matrix size, FOV, and slice thickness were 128×128 , 320–340 mm, and 5 mm, respectively. Twenty TRs were needed prior to acquisition in order to

reach steady-state conditions (labeled “transient” in Fig. 2). The total acquisition time of approximately 2.5 min for each component u_i results from 34 repetitive scans of 1.9608 s duration each ($[360 + 20 \text{ transient TRs}] \times 5.16 \text{ ms}$) performed during breath-hold at end-expiration followed by a short delay of approximately 2.5 s for respiration. Our standard protocol consisted of five experiments, one of which was a reference experiment conducted without vibration by sensitization along the slice selection direction. The other experiments were three MRE experiments with consecutive sensitization of all components u_i , followed by one conventional, retrospectively gated cine-MRI. The latter was acquired for comparison of wave data with intrinsic heart motion. To assess the variability of cardiac MRE, the protocol was applied twice in each volunteer with different image slice orientations in the short-axis view. The distance of both image slices was between 18 and 29 mm. In the following, these slice positions are referred to as slice position 1 and slice position 2 as shown in Fig. 3b.

RESULTS

Phantom Experiments

Figure 4a and b show transverse images of the magnitudes of shear waves induced (a) via plate actuator from the top

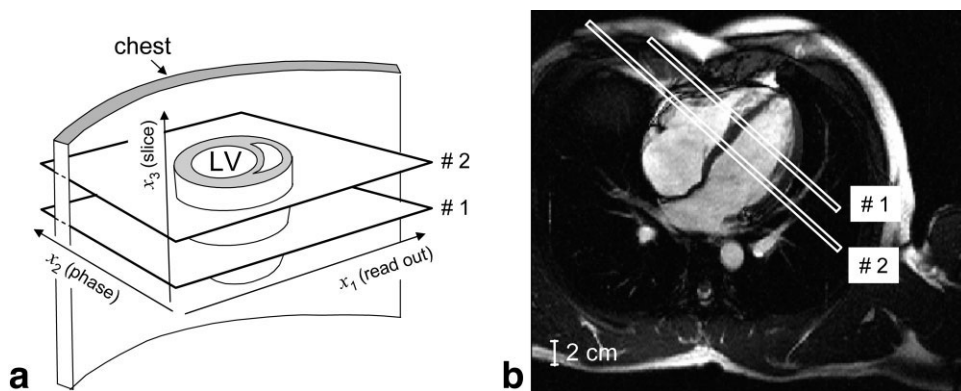


FIG. 3. **a**: Cartesian coordinate frame \mathbf{x} as defined by the imaging gradients along the directions of read, phase, and slice selection. The labels 1 and 2 refer to the image slice positions used in this study. **b**: A typical setup of the two image slice positions used in this study.

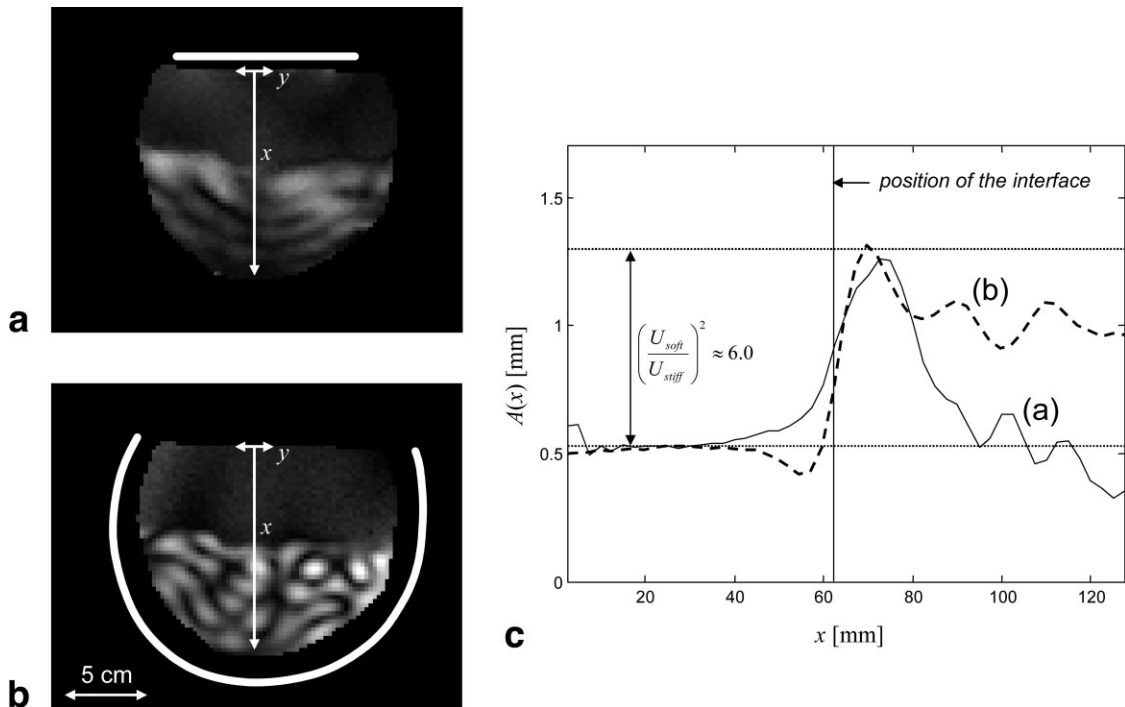


FIG. 4: Phantom experiment to demonstrate the effect of elastic heterogeneity on shear wave amplitudes. A two-layer phantom with horizontal interface and a higher stiffness in the upper than in the lower part was used for experimentally modeling spatial wave amplitude variations. The figure shows the magnitudes of wave amplitudes induced by a plate actuator from the top (a) and by the vessel walls (b) as demarcated by white lines. c: Profiles through a and b at the position of the arrows x , horizontally averaged along y . The dotted lines in c were used to estimate the change in shear wave amplitudes at the elastic interface.

and (b) via the surrounding container walls. It is clearly visible that bulk waves penetrate the material more uniformly in image b than in image a. The higher attenuation of the waves in Fig. 4a than in b can be attributed to the more localized wave excitation in image a, and to the higher degree of reverberations in image b due to the cylinder-shaped vibrating boundaries. Wave lengths measured were 120 ± 5 mm in the stiff gel and 22 ± 3 mm in the soft gel, yielding wave speeds of 3.9 ± 0.2 m/s and 0.7 ± 0.1 m/s, respectively. The resulting shear moduli are thus $\mu_{\text{stiff}} = 15.2 \pm 1.6$ kPa and $\mu_{\text{soft}} = 0.5 \pm 0.1$ kPa. As such, it follows from Eq. [3] that the expected wave amplitude ratio is 2.4 ± 0.2 . Figure 4c shows vertical profiles of the wave amplitude magnitudes through the phantom. The horizontal auxiliary lines shown in this figure indicate the degree of the amplitude difference at the interface position. The distance between the auxiliary lines is 0.77 mm, yielding an approximated amplitude ratio of 2.5, which confirms our modulus predictions made above. One important observation in this phantom study is the dependence of the wave amplitude ratio on the tissue penetration by the waves. While in Fig. 4a the ratio decreases sharply with distance from the interface, the ratio in b better preserves the information about elasticity differences beyond the interface. However, similar to what is seen in Fig. 4a, the correct amplitude ratio in b is best calculated by considering their maximum increase within a local window of ± 10 mm at the interface position. This supports the need for determining the position of the WAV effect prior to quantification of elasticity ratios as a means to account for attenuation.

In Vivo Wave Amplitude Variation

Figures 5 and 6 demonstrate the principles of data analysis in cardiac WAV-MRE compared to the simultaneously acquired oscillations in the chest of a volunteer. Figure 5a shows phase signal oscillations in the through-plane direction spatially averaged in two ROIs of similar size: one in the subcutaneous tissues of the upper chest, and the other determined by the systolic boundaries of the LV. The signal acquired without externally induced vibrations is represented by the thick line superimposed on the thin line representing the oscillations. The temporal resolution is equal to the TR of 5.16 ms. Visual comparison of the dynamics of oscillations in the chest and the myocardium reveals constant maximum wave amplitudes in the chest, while LV oscillation amplitudes change due to intrinsic myocardial motion, which is encoded in the reference signal. Figure 5b shows that noise is somewhat increased in the temporally filtered $\phi(t)$ compared to $\phi(t)$. However, the modulation of wave amplitudes over the cardiac cycle is better visualized in $\phi(t)$ than in $\phi(t)$. In order to demonstrate the phase oscillations of $\phi(t)$ in Fig. 5a, phase wraps were removed by conventional 2D phase unwrapping. In contrast, no phase unwrapping algorithm was used prior to calculating $\phi(t)$ from Eq. [4], as shown in Fig. 5b. As a result, the LV wave amplitude variations shown in Fig. 5a are enhanced while intrinsic motion is suppressed.

Quantification of the wave displacement pattern is demonstrated in Fig. 6, where U_j was calculated from $\phi(t)$ Eqs. [5] and [6]. In this figure, U_3 corresponds to data shown in Fig. 5, while U_1 , U_2 and the magnitude U are shown for

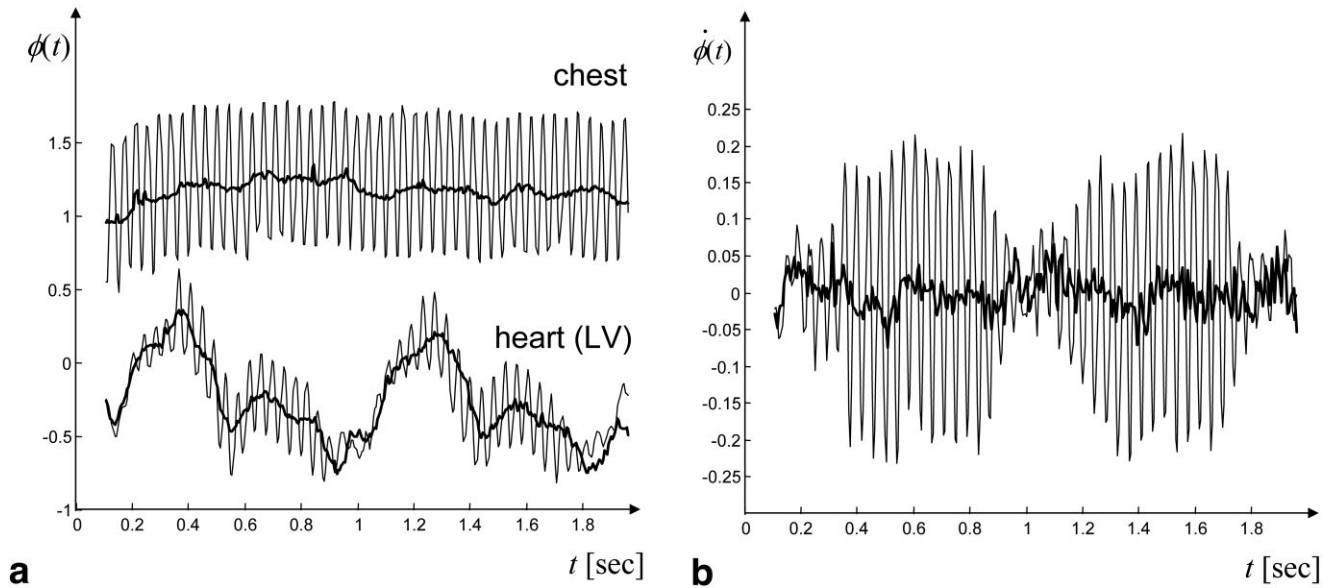


FIG. 5. **a**: Phase signal oscillations due to external vibrations seen in the heart and subcutaneous tissue of the upper chest of a volunteer (through-plane motion sensitization). **b**: Time derivative of $\phi(t)$ of the heart shown in part a. Fat lines indicate reference experiments without vibrations.

both the chest and LV ROIs. The temporal resolution of these graphs is 41.28 ms as determined by τ_v . These results indicate that the largest displacement component in the chest is U_2 , which is closer to the A-P vibration direction of the transducer than U and U_3 . Wave polarization is changed in the heart, where U_1 is approximately equal to U_2 . However, wave polarization was found to be different in each volunteer, which underscores the need to acquire all three wave components for quantifying elastic ratios.

Quantification of Elastic Ratios

Figure 7 shows images of the temporally averaged amplitudes (calculated from magnitude U), and their correlation with the gating function of diastole, S , for a

volunteer in both slice positions. In all experiments, significant wave intensity was observed over a large area of the chest. Wave penetration of the heart was found to be heterogeneous and different in all subjects. \hat{S} -maps indicate a significant wave amplitude alteration only within the heart and in larger blood vessels. The regions of blood flow tend to have negative \hat{S} -values, while

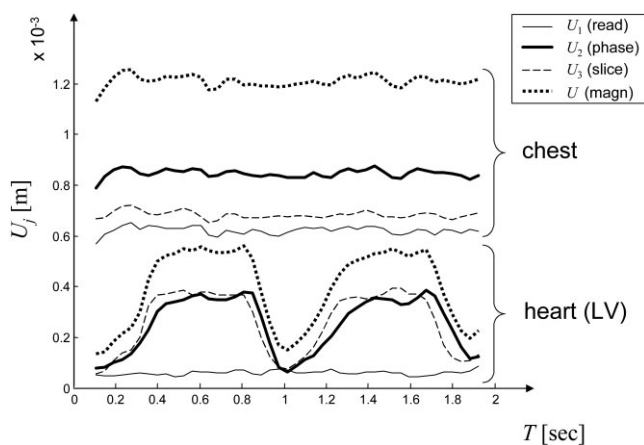


FIG. 6. Wave components in chest and heart averaged within the same ROIs used in Fig. 5a. The U_3 displacements (through-plane motion sensitization) were derived by inserting the $\phi(t)$ signals shown in Fig. 5a into Eqs. [4]–[6].

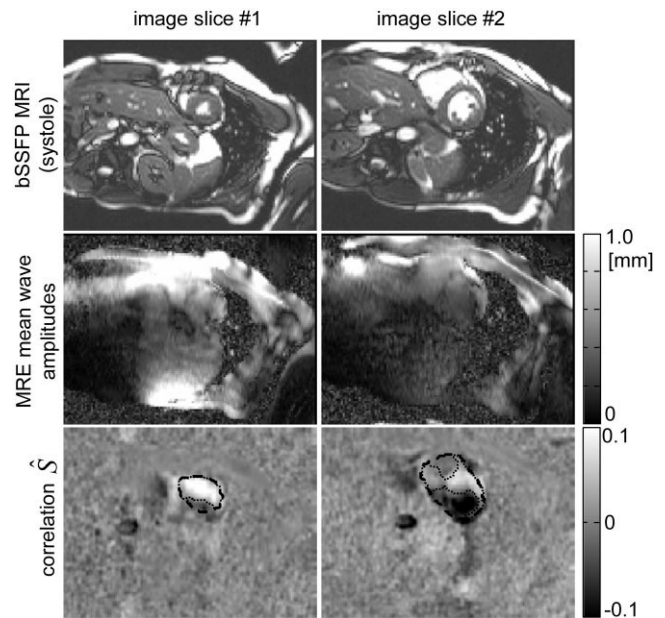


FIG. 7. Anatomical information in the two image slices used in this study, MRE wave displacement magnitudes, and \hat{S} correlations (cf., Fig. 1) in a volunteer. The MRE wave amplitudes show the temporal average of $U(T)$ during systole. Dashed lines plotted on \hat{S} images indicate outer boundaries of the entire heart during systole, while dotted lines demarcate the used ROI, which is defined by points with $\hat{S} > 0$ within the systolic region of the heart (see text for further details).

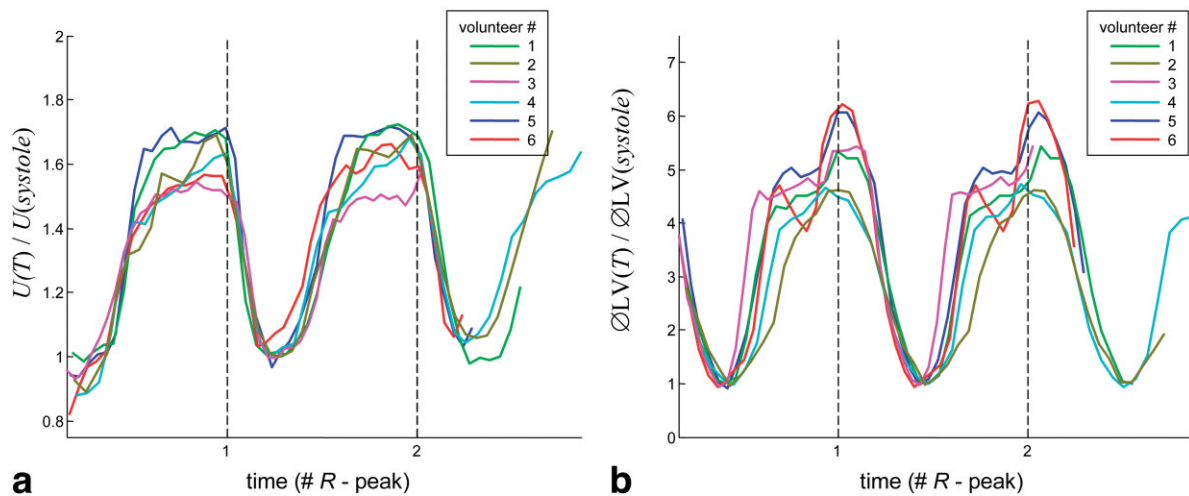


FIG. 8. Individual shear wave amplitudes $U(T)$ (a) and LV diameters (b) normalized by their values during systole and diastole, respectively. The time axis is relative to the individual ECG signals.

most of the myocardium has higher \hat{S} -values than surrounding noise. However, it is generally not possible to separate the myocardium from blood by means of \hat{S} because 1) there is blurring of heart boundaries due to intrinsic cardiac motion, and 2) the variation of shear wave amplitudes is not entirely localized to the position where the elasticity change occurs due to attenuation, as observed in the phantom experiments. The wave amplitude alterations within the blood may also be caused by surface and boundary effects from surrounding walls (20,28). Such effects combined with blood flow and wave attenuation render the quantification of elasticity ratios rather complex. Reproducible results were obtained by averaging WAV over the ROIs of image slices 1 and 2 given by $\hat{S} > 0$ and the systolic heart boundaries (see Fig. 7). This choice of ROI precludes points of negative WAV ($\hat{S} < 0$), which we attribute to intrinsic motion and blood flow. Accordingly, the WAV ratio between diastole and systole, $U(\text{diastole})/U(\text{systole})$, was determined at 1.58 ± 0.06 . Thus, the cardiac shear modulus variation, $\mu(\text{diastole})/\mu(\text{systole})$, was derived from $U(T)$ by Eq. [3], yielding a ratio of 6.3 ± 0.9 . The maximum WAV determined at points corresponding to $\max(\hat{S})$ was about 1.5 times higher with 2.45 ± 0.18 , which corresponds to a shear modulus ratio of 37.7 ± 10.6 .

Time Course of Amplitude Variations

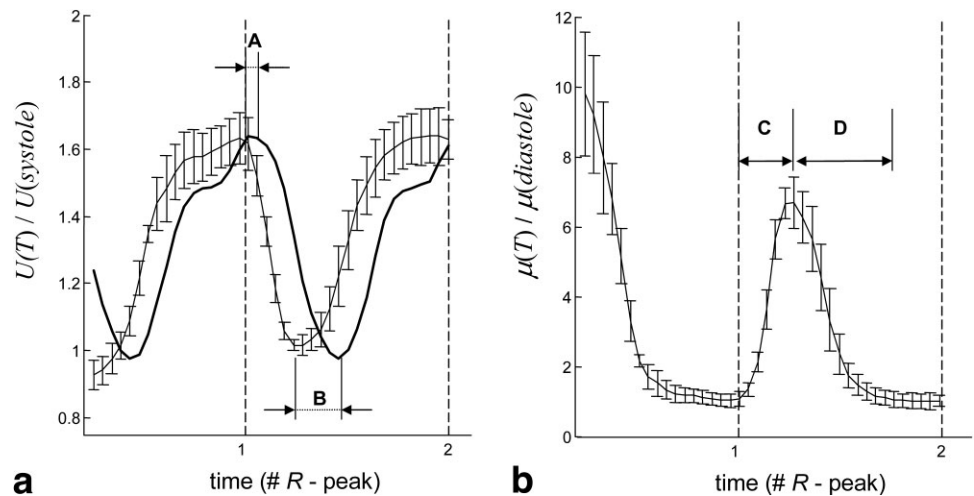
In Fig. 8a, the evolution of wave amplitude variations is plotted against a normalized time relative to the R -peaks of the ECG. It is seen that the wave amplitudes start to decline instantaneously at the beginning of systole, indicated by the R -peak. Comparison of the $U(T)$ curves with the relative diameter of the LV ($\delta LV(T)$, Fig. 8b) indicates that the decline of $U(T)$ precedes ventricular contraction. Individual data are given in Table 1. Delays between end-diastolic elasticity changes and heart motion are listed in column A of this table. These values show that myocardial stiffness increases at 75 ± 9 ms before geometrical changes are visible in the short-axis view, which indicates an isovolumetric tension phase. Column B lists the late systolic delay between elasticity change and motion. The increased delay of 159 ± 23 ms indicates that the ventricular contraction rate is slower than the myocardial tension increase rate during early systole. The last two columns of Table 1 list the time of muscle contraction and relaxation in each volunteer. Values of 204 ± 30 and 332 ± 38 ms underscore the asymmetry of these processes, which is also suggested by the graphs in Fig. 9. In this figure, the mean and standard deviation (SD) of all volunteer studies in slice 1 is represented by the amplitude ratio (a) and the modulus ratio (b). The aforementioned isovolumetric ten-

Table 1
Time Course of Wave Amplitude Variations and Duration of the Cardiac Cycle of Each Volunteer

Volunteer #	Cardiac Cycle	A	B	C	D
1	83	89 ± 10	137 ± 18	184 ± 12	392 ± 65
2	81	73 ± 4	137 ± 13	251 ± 6	287 ± 14
3	102	63 ± 12	152 ± 27	205 ± 18	349 ± 45
4	73	70 ± 10	164 ± 3	187 ± 22	312 ± 43
5	87	73 ± 26	166 ± 15	227 ± 18	303 ± 23
6	90	82 ± 64	197 ± 18	172 ± 13	347 ± 16
Mean	86 ± 10	75 ± 9	159 ± 23	204 ± 30	332 ± 38

All values are given as mean \pm SD ms. A: Delay between wave amplitude reduction and start of LV contraction. B: Difference between the minima of wave amplitudes and LV diameters. C: Time from R-wave to maximum myocardial tension. D: Tension relaxation time. These parameters were manually measured by three operators using the data displayed in Fig. 9. The bottom row gives the interindividual mean \pm SD.

FIG. 9. **a**: Mean values of the individual shear wave amplitudes shown in Fig. 8a (image slice 1) with error bars corresponding to the SD in six volunteers. The thick line represents the mean values of LV diameter in all volunteers (cf., part b). **b**: Mean values of all individual shear elasticity changes normalized to elasticity during diastole (error bars represent the SD) obtained from inserting the shear wave amplitude ratios in part a into Eq. [3]. The labels A–D correspond to columns 3–6 in Table 1.



sion and late systolic motion delay are clearly visible in Fig. 9a (in comparison to the mean \emptyset LV curve). Initial low ratios in Fig. 9a and high ratios in Fig. 9b are presumably caused by the transient phase-signal response of steady-state MRE as visible in the chest signal of Fig. 5a.

DISCUSSION

It was demonstrated that WAV-MRE enables noninvasive measurement of myocardial elasticity changes. Few ultrasound studies in the literature have addressed myocardial elastography using the inherent contractile function of the heart as the mechanical stimulus (29,30). Kanai (19) measured viscoelastic values of the myocardium ($\mu = 24\text{--}30$ kPa) by exploiting wall vibrations after aortic valve closure. Rump et al. (17) derived preliminary elastic parameters between 5 and 27 kPa at four instances during the cardiac cycle using, for the first time, external vibrations in conjunction with MRI. In contrast, WAV-MRE measures the dynamics of relative elasticity changes, which is hard to compare with absolute elasticity values measured at single (19) or very few time points (17). It is well established that the change in myocardial stiffness is directly related to the change in intraventricular pressure (31). The maximum elasticity variation measured in our study (37.7 ± 10.6) is comparable to interventional catheter results showing an increase in LV pressure of about a factor of 33 ± 11 in normal male controls (21,22). Furthermore, time A (75 ± 9 ms) given in Table 1 corresponds to the invasively measured isovolumetric contraction time, which is known as the delay between the increase in intraventricular pressure and the decrease in LV diameter (or volume) (32). Very similar values were obtained by echocardiography (33) and invasive catheter measurement (32), indicating that the experiment presented here is potentially capable of noninvasively mapping ventricular pressure evolution during the cardiac cycle. Measurement of wave amplitude modulations with sufficient time resolution is an important step in cardiac MRE. The fractional MRE sequence proposed here enabled us to acquire eight phase images during one tissue vibration cycle. However, this excellent temporal resolution of almost 5 ms came at the expense of the SNR, which was reduced by a large

bandwidth together with an incompletely spoiled residual magnetization. Furthermore, extensive k -space segmentation required repeated breath-holding during each phase-encoding step. In a future variation of the proposed protocol, the number of images can be reduced so that the recorded oscillations do not exceed one cardiac cycle. Further optimization with regard to k -space sampling and parallel imaging might reduce acquisition times to less than 20 s, which would considerably improve the applicability of cardiac MRE in patients as it eliminates the need for repeated breath-hold sampling. For possible future patient studies, it is worthwhile to mention that none of the volunteers reported discomfort from mechanical actuation. Several volunteers described the low-frequency vibration of the chest as a moderate buzz comparable to vibrations induced by bicycling on cobblestone. The noise level of the wave source was below that of the imaging gradients.

The sensitivity of shear vibration amplitudes to elasticity variations was demonstrated in a phantom. Although elasticity varies only spatially in this simple model, the principal findings also apply to the heart. Figure 4a and b indicate the influence of wave reflections, reverberations, and damping on the magnitudes of the wave amplitudes. In the phantom, determination of the elasticity ratio was only possible by averaging the wave amplitudes within a specific ROI in the vicinity of the interface. The maximum amplitude ratio was found to be an appropriate measure of the leap in elasticity. Further research is required to determine the degree of certainty to which the maximum WAV effect represents true elasticity ratios according to Eq. [3]. Clearly, wave reflections at tissue boundaries influence wave amplitudes and thus the derived elasticity ratios as seen in Fig. 4. In addition, the elasticity information carried by the wave may be diluted by wave damping. Therefore, we related the positions of the ROIs to the WAV effect given by \hat{S} . However, since no heart motion or deformation is considered in our theory, \hat{S} provides only a rough approximation of the regional amplitude effect. Thus the quantification routine used may be improved by accounting for geometrical changes of the heart, i.e., by correlating U and S along predetermined spatiotemporal pathways.

The evaluation of vibration amplitudes in deforming objects remains the subject of ongoing work.

The interpretation of the WAV effect was based on several assumptions, which allowed us to reduce the complexity of myocardial MRE to an analysis of wave amplitude ratios. Major simplifications were achieved by assuming constant wave intensity, linear elastic and isotropic material behavior, and plane shear wave propagation. Consequently, our current strategy of data evaluation is only a starting point. A further in-depth analysis is necessary to better understand the observed effect. More accurate treatment of myocardial vibration requires a formulation that considers wave propagation through a medium undergoing finite elastic deformation.

To consider anisotropy, constitutive equations developed for shear-wave-based elastography of skeletal muscle can be used (Eqs. [A3]–[A5]) (34). With this change, wave propagation speed is determined by a combination of three elastic constants. These constants are the parallel shear modulus, the perpendicular shear modulus, and the ratio of parallel and perpendicular Young's moduli relative to the muscle fiber direction. This more elaborate anisotropic model can predict the spatial variations of the elastic constants, since the fiber orientation of the myocardial tissue in the ventricular wall changes as a function of the position. Assuming a shear modulus parallel to the muscle fibers to be five times larger than the perpendicular shear modulus (34) yields a fivefold elasticity change in case of a 90° flip of the principal fiber direction due to cardiac motion. This effect on $\mu(\text{diastole})/\mu(\text{systole})$ represents the maximum shear modulus alteration solely resulting from myocardial anisotropy, i.e., no muscle contraction is taken into account.

In summary, the proposed technique of cardiac WAV-MRE yields elasticity ratios for different phases of the cardiac cycle. This dynamic information on shear modulus variation reveals elastodynamic processes of the heart that are otherwise attainable only by invasive methods. Thus, WAV-MRE may become a valuable noninvasive modality for the diagnosis of diseases associated with dysfunctional alterations in myocardial stiffness.

ACKNOWLEDGMENT

We thank Dagmar Krefting for stimulating discussions on correlation analysis.

APPENDIX

Strain Energy Flux

The density of deformation energy in an elastic body is the sum of two terms representing the kinetic (E_{kin}) and the potential (strain) energy density (E_{pot}):

$$E = E_{kin} + E_{pot}$$

$$E_{kin} = \frac{1}{2}\rho\dot{u}_i\dot{u}_i; E_{pot} = \frac{1}{2}C_{ijkl}\frac{\partial u_i\partial u_k}{\partial x_j\partial x_l} \quad [A1]$$

Indices $i, j, k, l \in \{1, 2, 3\}$ denote tensor elements subjected to Einstein's summation rule. \mathbf{x} and \mathbf{u} represent vectors of the medium's position and displacement, while \mathbf{C} is the elasticity tensor. The change in energy enclosed in the volume, V , of an elastically deformed medium occurs from the flux of a vector \mathbf{F} through the surface bounding the volume as given by:

$$\int_V \dot{E}dV = \int_V \left(\rho\dot{u}_i\ddot{u}_i + C_{ijkl}\frac{\partial\dot{u}_j\partial u_k}{\partial x_j\partial x_l} \right) dV = - \int_{\Sigma} F_m d\Sigma_m. \quad [A2]$$

In this equation, F_m represents the flux of energy across the surface Σ where $d\Sigma_m$ is the differential surface area whose normal vector is n_m . Applying the product rule to the strain energy term in Eq. [A2] and using Gauss's theorem, it was found that (35):

$$F_j = - C_{ijkl}\frac{\partial u_k}{\partial x_l}\dot{u}_i, \quad [A3]$$

which applies to deformed materials in the equilibrium of external forces. Tissue weight is assumed to be counterbalanced by connective tissues. For an isotropic elastic material, \mathbf{F} can be expressed in terms of Lamé coefficients λ and μ :

$$F_j = - \lambda\frac{\partial u_k}{\partial x_k}\delta_{ij}\dot{u}_i - 2\mu\frac{\partial u_i}{\partial x_j}\dot{u}_i. \quad [A4]$$

Energy Transport by Elastic Waves

The movement of energy by elastic waves is governed by three eigenmodes (M), which are defined with respect to wave propagation direction n_j as one longitudinal (compressional) mode ($M = L$) and two transverse (shear) modes ($M = T$). In isotropic materials both transverse wave modes are degenerated, leaving two distinguishable phase velocities, c_L and c_T :

$$\rho c_L^2 = \lambda + 2\mu \quad [A5]$$

$$\rho c_T^2 = \mu$$

Their eigenvectors, \mathbf{U}_M , define the polarization of the wave modes, u_M :

$$u_{jM} = U_{jM}\exp\left(i\omega\left[\frac{x_k n_k}{C_M} - t\right]\right); M = L, T. \quad [A6]$$

Insertion into Eq. [A4] yields the energy-density flux:

$$F_{jM} = \rho c_M u_{j(M)^2} \omega^2; M = L, T. \quad [A7]$$

Theoretically, two modes of energy flux occur in isotropic materials: one related to compressional waves and the other related to shear waves. In reality, both modes are linearly combined depending on the propagation direction

and the polarization of the waves, which in turn are determined by the position, shape, and polarization of the wave source as well as by tissue boundaries. Furthermore, in anisotropic materials, the orientation of the principal frame of elasticity relative to the waves has to be considered in addition to a third, distinct transverse wave mode. Analytical expressions of shear wave modes in transverse isotropic and incompressible media are taken from Ref. 34.

REFERENCES

- Stewart S, MacIntyre K, Hole DJ, Capewell S, McMurray JJ. More "malignant" than cancer? Five-year survival following a first admission for heart failure. *Eur J Heart Fail* 2001;3:315–322.
- Bleumink GS, Knetsch AM, Sturkenboom MC, Straus SM, Hofman A, Deckers JW, Wittman JC, Stricker BH. Quantifying the heart failure epidemic: prevalence, incidence rate, lifetime risk and prognosis of heart failure. The Rotterdam Study. *Eur Heart J* 2004;25:1614–1619.
- McMurray JJ, Pfeffer MA. Heart failure. *Lancet* 2005;365:1877–1889.
- Burkhoff D, Mirsky I, Suga H. Assessment of systolic and diastolic ventricular properties via pressure-volume analysis: a guide for clinical, translational, and basic researchers. *Am J Physiol Heart Circ Physiol* 2005;289:H501–H512.
- Gaasch WH, Zile MR. Left ventricular diastolic dysfunction and diastolic heart failure. *Ann Rev Med* 2004;55:373–394.
- Wachter R, Pieske B. [Restrictive cardiomyopathy]. *Herz* 2005;30:558–564.
- Finn JP, Nael K, Deshpande V, Ratib O, Laub G. Cardiac MR imaging: state of the technology. *Radiology* 2006;241:338–354.
- Aurigemma GP, Zile MR, Gaasch WH. Contractile behavior of the left ventricle in diastolic heart failure: with emphasis on regional systolic function. *Circulation* 2006;113:296–304.
- Thomas JD, Popovic ZB. Assessment of left ventricular function by cardiac ultrasound. *J Am Coll Cardiol* 2006;48:2012–2025.
- Kasner M, Westermann D, Steendijk P, Gaub R, Wilkenschoff U, Weitemann K, Hoffmann W, Poller W, Schultheiss HP, Pauschinger M, Tschope C. Utility of Doppler echocardiography and tissue Doppler imaging in the estimation of diastolic function in heart failure with normal ejection fraction: a comparative Doppler-conductance catheterization study. *Circulation* 2007;116:637–647.
- Axel L, Dougherty L. MR imaging of motion with spatial modulation of magnetization. *Radiology* 1989;171:841–845.
- Osman NF, Kerwin WS, McVeigh ER, Prince JL. Cardiac motion tracking using CINE harmonic phase (HARP) magnetic resonance imaging. *Magn Reson Med* 1999;42:1048–1060.
- Jung B, Zaitsev M, Hennig J, Markl M. Navigator gated high temporal resolution tissue phase mapping of myocardial motion. *Magn Reson Med* 2006;55:937–942.
- Fung Y. *Biomechanics: mechanical properties of living tissue*. New York: Springer-Verlag; 1993.
- Muthupillai R, Lomas DJ, Rossman PJ, Greenleaf JF, Manduca A, Ehman RL. Magnetic resonance elastography by direct visualization of propagating acoustic strain waves. *Science* 1995;269:1854–1857.
- Parker KJ, Huang SR, Musulin RA, Lerner RM. Tissue response to mechanical vibrations for "sonoelasticity imaging". *Ultrasound Med Biol* 1990;16:241–246.
- Rump J, Klatt D, Braun J, Warmuth C, Sack I. Fractional encoding of harmonic motions in MR elastography. *Magn Reson Med* 2007;57:388–395.
- Rump J, Warmuth C, Braun J, Sack I. Phase preparation in steady-state free precession MR elastography. *Magn Reson Imaging* 2008;26:228–235.
- Kanai H. Propagation of spontaneously actuated pulsive vibration in human heart wall and in vivo viscoelasticity estimation. *IEEE Trans Ultrason Ferroelectr Freq Control* 2005;52:1931–1942.
- Achenbach JD. *Wave propagation in elastic solids*. Amsterdam: Elsevier; 1999.
- Hayward CS, Kalnins WV, Kelly RP. Gender-related differences in left ventricular chamber function. *Cardiovasc Res* 2001;49:340–350.
- Zile MR, Baicu CF, Gaasch WH. Diastolic heart failure—abnormalities in active relaxation and passive stiffness of the left ventricle. *N Engl J Med* 2004;350:1953–1959.
- Papazoglou S, Hamhaber U, Braun J, Sack I. Horizontal shear wave scattering from a nonwelded interface observed by magnetic resonance elastography. *Phys Med Biol* 2007;52:675–684.
- Hamhaber U, Sack I, Papazoglou S, Rump J, Klatt D, Braun J. Three-dimensional analysis of shear wave propagation observed by in vivo magnetic resonance elastography of the brain. *Acta Biomater* 2007;3:127–137.
- Klatt D, Asbach P, Rump J, Papazoglou S, Somasundaram R, Modrow J, Braun J, Sack I. In vivo determination of hepatic stiffness using steady-state free precession magnetic resonance elastography. *Invest Radiol* 2006;41:841–848.
- Asbach P, Klatt D, Hamhaber U, Braun J, Somasundaram R, Hamm B, Sack I. Assessment of liver viscoelasticity using multifrequency MR elastography. *Magn Reson Med* 2008;60:373–379.
- Crawley AP, Wood ML, Henkelman RM. Elimination of transverse coherences in FLASH MRI. *Magn Reson Med* 1988;8:248–260.
- Woodrum DA, Romano AJ, Lerman A, Pandya UH, Brosh D, Rossman PJ, Lerman LO, Ehman RL. Vascular wall elasticity measurement by magnetic resonance imaging. *Magn Reson Med* 2006;56:593–600.
- Konofagou EE, D'Hooge J, Ophir J. Myocardial elastography—a feasibility study in vivo. *Ultrasound Med Biol* 2002;28:475–482.
- Luo J, Fujikura K, Homma S, Konofagou EE. Myocardial elastography at both high temporal and spatial resolution for the detection of infarcts. *Ultrasound Med Biol* 2007;33:1206–1223.
- Glantz SA, Kernoff RS. Muscle stiffness determined from canine left ventricular pressure-volume curves. *Circ Res* 1975;37:787–794.
- Gault JH, Ross Jr J, Braunwald E. Contractile state of the left ventricle in man: instantaneous tension-velocity-length relations in patients with and without disease of the left ventricular myocardium. *Circ Res* 1968;22:451–463.
- Naqvi TZ, Neyman G, Broyde A, Mustafa J, Siegel RJ. Comparison of myocardial tissue Doppler with transmitral flow Doppler in left ventricular hypertrophy. *J Am Soc Echocardiogr* 2001;14:1153–1160.
- Papazoglou S, Rump J, Braun J, Sack I. Shear-wave group-velocity inversion in MR elastography of human skeletal muscle. *Magn Reson Med* 2006;56:489–497.
- Fedorov FI. *Theory of elastic waves in crystals*. New York: Plenum; 1968.